# Unified Framework for the Joint Super-Resolution and Registration of Multiangle Multi/Hyperspectral Remote Sensing Images

Hang Chen, Hongyan Zhang ⓘ, *Senior Member, IEEE*, Juan Du ⓘ, and Bin Luo ⓘ

*Abstract*—In this article, a unified framework based on rank minimization (UFRM) is proposed for use with multiangle multi/hyperspectral remote sensing images, which simultaneously integrates image super-resolution reconstruction (SRR) and image registration. With the complementary information of different angle images and the high correlation between each band of the multi/hyperspectral images, a new image observation model is established to describe the mathematical degradation process of the observed low-resolution multiangle multi/hyperspectral images from the desired high-resolution (HR) multi/hyperspectral image. Based on the rank-one structure of the multiangle images, each observed image is decomposed into a foreground image for each angle image, and a background image, which is shared among all the multiangle images. A multichannel total variation constraint is applied to the target HR background image, with the consideration of the high correlation of different bands. Finally, an alternating minimization optimization strategy is utilized to resolve the joint cost function, which consists of the unknown image registration transformation parameters and the desired reconstruction image. As a result, the UFRM method can simultaneously achieve image registration and SRR. A number of experiments were conducted, which confirmed the superior performance of the proposed method.

*Index Terms*—Multiangle, multi/hyperspectral, registration, super-resolution, rank-one.

## I. INTRODUCTION

MANY imaging systems are now equipped with multiangle multi/hyperspectral abilities, which opens up new possibilities for remote sensing applications such as 3-D reconstruction [1], [2], image classification [3]–[6], object detection [7]–[9], change detection [10], and so on. Due to the tradeoff between the spectral and spatial perspectives of multi/hyperspectral images, the spatial resolution of multiangle multi/hyperspectral images is often coarse. This phenomenon limits the further development of the remote sensing applications to a large extent. In order to improve the spatial resolution of the observed images, one effective solution is to develop more advanced optical imaging devices, which is referred to as the "hardware approach" [11]. However, there is always a technical limitation with regard to the hardware approach. In addition, the huge economic cost is another obstacle. Thus, it is necessary to develop data postprocessing techniques to improve the spatial resolution of remote sensing images.

Super-resolution reconstruction (SRR) is a technique that can be used to reconstruct a higher resolution image from several observed low-resolution (LR) images. Generally speaking, SRR can be categorized as multiframe or single-frame, based on the input LR images. Considering that our attention is focused on multiangle multi/hyperspectral images, only multiframe SRR methods are discussed in this article. The idea of multiframe SRR was first proposed by Tsai and Huang [12] to improve the spatial resolution of Landsat Thematic Mapper (TM) images. Since then, superresolution has attracted a lot of interest from researchers, and there have been various classical reconstruction frameworks proposed, such as maximum *a posteriori* (MAP) image reconstruction [13], [14], projection onto convex sets (POCS) [15], non-uniform interpolation [16], maximum likelihood reconstruction [17], the iterative back-projection approach (IBP) [18], mixed maximum MAP/POCS [19], and so on. Generally speaking, the key problem of multiframe SRR is how to seek the complementary information, which comes from the subpixel displacements among the multiple observed LR images. That is to say, the precondition for the SRR of remote sensing images is that there is similar but not totally identical information existing between the observed images over the same imaging scene. In the following, we discuss three cases of LR remote sensing images for SRR.

1) Shift-controlled case. The most successful remote sensing SRR case is the SPOT-5 imaging system. This system shifts half a sampling interval in the horizontal and vertical directions by a double charge-coupled device (CCD) linear array, which obtains two 5-m resolution images, and then produces an approximately 2.5-m resolution high-resolution (HR) image through SRR

Hang Chen, Hongyan Zhang, and Bin Luo are with the State Key Laboratory of Information Engineering in Surveying, Mapping, and Remote Sensing, Wuhan University, Wuhan 430079, China (e-mail: hangchen@whu.edu.cn; zhanghongyan@whu.edu.cn; luob@whu.edu.cn).

Juan Du is with the School of Remote Sensing and Information Engineering, Wuhan University, Wuhan 430079, China (e-mail: dujuan_rs@whu.edu.cn).

processing [20], [21]. However, this imaging system requires precise design of the hardware system.

2) Multitemporal case. With its high temporal resolution observation capability, the Moderate Resolution Imaging Spectroradiometer (MODIS), which is carried on the TERRA/Aqua satellites, can acquire imagery of the same scene every 1 or 2 d. It can therefore quickly provide a sequence of observed LR images with a short time span. An operational SRR algorithm was first proposed by Shen *et al*. [22] for MODIS images. In addition, an SRR method based on a universal hidden Markov tree model for remote sensing data was proposed by Li *et al*. [23] and tested with Landsat 7 panchromatic images captured on different dates. It is clear that the multitemporal remote sensing imaging case can provide the subpixel-displaced image sequence for the SRR task. However, there may be a gap of several days, or even a much longer time interval, between multitemporal satellite images. Therefore, the imaging scene or weather conditions can change a lot in this period, which poses great difficulties for the image registration and SRR of multitemporal remote sensing images.

3) Multiangle case. A multiangle remote sensing imaging system can obtain multiple images at different angles, within a short time span, such that the imaging scene and weather conditions hardly change at all [24]. Subpixel displacement also exists in the multiangle images of the same scene. Therefore, multiangle images are more suitable for SRR than multitemporal images. In recent years, the SRR of remote sensing images has mainly focused on multiangle image sequences [24]–[27].

Conventionally, the multiframe SRR procedure usually consists of two steps: image registration and image reconstruction. The precise image registration is a prerequisite and plays an important role in the generation of the final super-resolved image [28], [29]. To date, several image registration algorithms have been proposed to estimate the subpixel displacements between multiangle images. In [25], an effective multiangle image registration method was proposed using a physical sensor model. However, supplementary data such as a digital elevation model (DEM) are required for this method, which cannot always be obtained, especially for certain imaging systems. Ma *et al*. [26] proposed an automatic subpixel image registration method for CHRIS/PROBA multiangle images. However, high-precision SIFT control points are a precondition in the first step, which are often difficult to obtain because of the resolution change and blurring between the multiangle images. In addition, Hu *et al*. [27] proposed a multiangle image registration method that exploits the low-rank structure of multiangle remote sensing images. In [30], an affine SIFT-based local registration method was proposed by Wang *et al*. for remote sensing images, where a framework for localization in the image registration was developed and the local registration accuracy was strengthened. Furthermore, Laghrib *et al*. [31] proposed a spatially weighted second-order super-resolution method, where all the LR images are registered by a hyperelastic registration method, which is used to handle the subpixel errors between the unregistered images.

As for HR image reconstruction from the available multiangle remote sensing images, a number of algorithms have also been developed. For example, Chan *et al*. [32] conducted SRR experiments with Delaunay triangulation based nonuniform interpolation. In [33], ZY-3 multiangle images were used to implement SRR, where a Fourier transformation method is utilized to register the ZY-3 images. Ma *et al*. [34] proposed an operational super-resolution algorithm for multiangle WorldView-2 remote sensing images, where the local geometric distortion and photometric disparity are considered in the image registration stage, and an L1-norm data fidelity item and total variation regularization are utilized in the SRR model. In [35], Ma *et al*. proposed an SRR method for multiangle remote sensing images, which considers the concept of kernel-based regression. In this method, the local image patch is approximated by an N-term Taylor series, and a robust fitting procedure is also adopted. However, one shortcoming of all these methods is that they do not consider the resolution variations of the multiangle images. Galbraith *et al*. [36] noted that the spatial resolution of different angle images shows a slight difference, and the spatial resolution of an off-nadir image is lower than that of the nadir image. Hence, the contributions of the different angle images to the reconstructed image should be considered. Zhang *et al*. [21] proposed an adaptive-weighted super-resolution method, which considers the resolution variations of the multiangle images, where the different contributions of the multiangle LR images are reflected by different weights.

However, due to the presence of aliasing in the observed multiangle LR images, serious subpixel errors will still exist for most of the existing registration algorithms for aliased images [37]. Several attempts have been made to reduce the effect of registration errors. Among them, one important strategy is to build a unified framework for simultaneous image registration and image reconstruction. This approach involves conducting the image registration on the basis of the super-resolved images, and can lead to a better registration performance [37]. In [38], Gilles *et al*. proposed a joint image alignment and reconstruction method for multiangle panchromatic images. This method joins the processes of image registration and image reconstruction together, which avoids the error propagation in the image registration procedure and improves the quality of the reconstruction result. Gilles *et al*. [38] also noted that each observed image can be modeled as the sum of a background image and a foreground image. The background image is common to all the observed images, but undergoes geometric transformation. The foreground images differ from one angle image to another, and they are used to model the possible occlusions between the different angle images. Thus, this method takes the mutual dependency of the image registration and image reconstruction stages into account, and can achieve a state-of-the-art SRR performance for multiangle panchromatic images. However, directly applying the joint image registration and SRR reconstruction method to the multiangle multi/hyperspectral images is problematic due to the high correlation between the different bands of the multi/hyperspectral images. Dealing with these bands separately does not fully exploit the correlation between them, and results in spectral artifacts in the final super-resolved hyperspectral image.

In view of this, we propose a unified framework based on rank minimization (UFRM) for the joint super-resolution and registration of multiangle multi/hyperspectral remote sensing images, which considers the rank-one structure of the multiangle images and the spectral information of the multi/hyperspectral images at the same time. Firstly, the observation model for the multiangle multispectral images is constructed, and the rank-one structure of the multiangle multi/hyperspectral images is explored by lexicographically ordering the 3-D data cube as a 2-D matrix. Secondly, a unified MAP framework is established, which integrates the image super-resolution and registration procedures. Thirdly, considering the high correlation between the different bands of the images, a multichannel total variation (MTV) [39] constraint is applied. In this model, all the band information is treated as an entirety, rather than band-by-band, which can exploit the spectral characteristics between bands more deeply. With the established framework, the image registration parameters are iteratively updated, along with the progressively estimated HR images, in a cyclic optimization procedure, which can reduce the negative effect of image registration errors. The UFRM algorithm is aimed at reinforcing the interdependence of the image registration parameters and the HR multi/hyperspectral images in a mutually beneficial manner, and is an extension of our previous conference work [24].

The rest of this article is organized as follows. In Section II, we explain the observation model for multiangle multi/hyperspectral images. The unified super-resolution framework is then explained in detail, as well as the optimization algorithm. The flowchart of the unified super-resolution framework is also summarized. In Section III, we describe the experiments conducted with WorldView-2 and CHRIS/PROBA images, and an experimental analysis is provided. Finally, Section IV concludes the article and discusses our future work.

## II. METHODS

### A. Observation Model

The image observation model is used to simulate the imaging degradation process of the remote sensing imaging system, and to describe the mathematical relationship between the ideal HR image and the observed LR images. The SRR procedure is the inverse process of the observation process, and is aimed at reconstructing the desired HR images from the available observations. Therefore, constructing the observation model is a prerequisite for the SRR reconstruction process. We first study the image observation model in the traditional multiangle panchromatic case, and then extend this model to the multiangle multi/hyperspectral case. The image acquisition process is inevitably confronted with degradation issues, including motion effects, blurring, noise, and downsampling. We let the underlying HR image be denoted as $\mathbf{x}$, and $\mathbf{y}_k$ denotes the $k$th LR angle image. If we assume that each observed LR image is contaminated by additive noise, then the observation model can be represented as

$$\mathbf{y}_k = \mathbf{D}_k\mathbf{B}_k\mathbf{M}_k\mathbf{x} + \mathbf{n}_k \quad k = 1, 2, 3, \ldots, p \tag{1}$$

where the size of $\mathbf{x}$ is $L_1 N_1 L_2 N_2 \times 1$. Letting $L_1$ and $L_2$ denote the downsampling factors in the horizontal and vertical directions, respectively, each observed LR image $\mathbf{y}_k$ has the size $N_1 N_2 \times 1$. $\mathbf{n}_k$ represents the $N_1 N_2 \times 1$ noise vector. $p$ is the total number of multiangle images. $\mathbf{M}_k$ is the warp matrix and $\mathbf{B}_k$ is the blur matrix, which have the same size of $L_1 N_1 L_2 N_2 \times L_1 N_1 L_2 N_2$. $\mathbf{D}_k$ is an $N_1 N_2 \times L_1 N_1 L_2 N_2$ downsampling matrix.

In this article, an improved observation model for multiangle multi/hyperspectral remote sensing images is proposed. Firstly, we study the new observation model in the single-band panchromatic case [38]. Each observed image is modeled as the sum of a background image and a foreground image. The background image of the different angle images undergoes geometric transformation. The foreground images differ from one observed image to another, and are used to model the possible occlusions of the scene. Therefore, the observed LR images can be represented as

$$\mathbf{Y} = \mathbf{Y}_F + \mathbf{Y}_B + \mathbf{N} \tag{2}$$

where $\mathbf{Y} = [\mathbf{y}_1, \mathbf{y}_2, \ldots, \mathbf{y}_p]^{\mathrm{T}}$ is the observed multiangle images. $\mathbf{Y}_F = [\mathbf{y}_{1F}, \mathbf{y}_{2F}, \ldots, \mathbf{y}_{pF}]^{\mathrm{T}}$ is the foreground image of the observed images and $\mathbf{Y}_B = [\mathbf{y}_{1B}, \mathbf{y}_{2B}, \ldots, \mathbf{y}_{pB}]^{\mathrm{T}}$ is the background image of the observed images. $\mathbf{N}$ is the Gaussian noise. This procedure is shown in Fig. 1. It is known that all the different angle images share the same land surface objects. With the background and foreground decomposition, it is assumed that the background images of the different angle images correspond to similar but not identical components, and can thus be utilized for super-resolution. As for the foreground, each foreground component is unique for each angle image, and the foreground components usually represent the occlusions. Therefore, interpolation is conducted for the foreground images to match the size of the super-resolved background images.

According to (1), the expansion of (2) is written as

$$
\begin{bmatrix} \mathbf{y}_1 \\ \mathbf{y}_2 \\ \vdots \\ \mathbf{y}_p \end{bmatrix} = \begin{bmatrix} \mathbf{D}_1\mathbf{B}_1 & 0 & \cdots & 0 \\ 0 & \mathbf{D}_2\mathbf{B}_2 & \vdots & \vdots \\ \vdots & \cdots & \ddots & \vdots \\ 0 & \cdots & \cdots & \mathbf{D}_p\mathbf{B}_p \end{bmatrix} \begin{bmatrix} \mathbf{x}_1 \\ \mathbf{x}_2 \\ \vdots \\ \mathbf{x}_p \end{bmatrix}
$$
$$
+ \begin{bmatrix} \mathbf{D}_1\mathbf{B}_1\mathbf{M}_1 & 0 & \cdots & 0 \\ 0 & \mathbf{D}_2\mathbf{B}_2\mathbf{M}_2 & \vdots & \vdots \\ \vdots & \cdots & \ddots & \vdots \\ 0 & \cdots & \cdots & \mathbf{D}_p\mathbf{B}_p\mathbf{M}_p \end{bmatrix}
$$
$$
\times \begin{bmatrix} \mathbf{x}_{01} \\ \mathbf{x}_{02} \\ \vdots \\ \mathbf{x}_{0p} \end{bmatrix} + \begin{bmatrix} \mathbf{n}_1 \\ \mathbf{n}_2 \\ \vdots \\ \mathbf{n}_p \end{bmatrix} \tag{3}
$$

where $\mathbf{x}_{01}, \mathbf{x}_{02}, \ldots, \mathbf{x}_{0p}$ represent the super-resolved HR background image with dewarping, deblurring, and upsampling for each angle, respectively. $\mathbf{x}_1, \mathbf{x}_2, \ldots, \mathbf{x}_p$ denote the interpolated
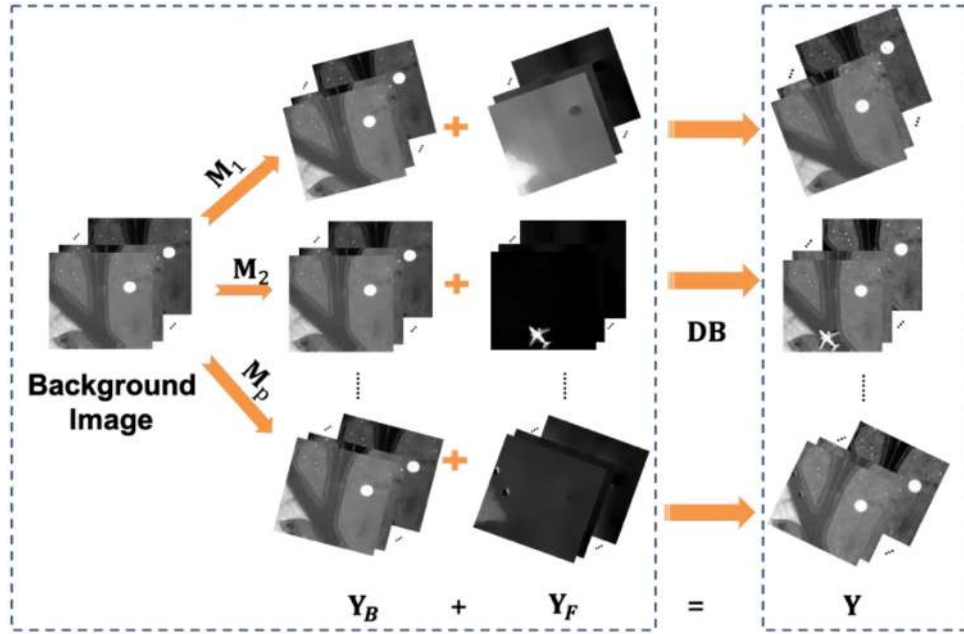
Fig. 1.     Degradation procedure for multiangle multi/hyperspectral images.

HR foreground images by only taking deblurring and upsampling into consideration. All the background images and foreground images have the same size of $L_1 N_1 L_2 N_2 \times 1$. If we stack all the HR background images as columns of a matrix, i.e., $[\mathbf{x}_{01}\ \mathbf{x}_{02}\ \ldots\ \mathbf{x}_{0p}]$, it is clear that this matrix will have a low-rank structure. That is to say, the HR background image is common to all the angles and, in ideal circumstances, the $p$ background images $\mathbf{x}_{01}, \mathbf{x}_{02}, \ldots, \mathbf{x}_{0p}$ should be all the same, so that the matrix $[\mathbf{x}_{01}\ \mathbf{x}_{02}\ \ldots\ \mathbf{x}_{0p}]$ is approximately rank-one. According to this assumption, $\mathbf{Y}_B$ can be expressed as

$$\mathbf{Y}_B = \begin{bmatrix} \mathbf{D}_1\mathbf{B}_1\mathbf{M}_1 \\ \mathbf{D}_2\mathbf{B}_2\mathbf{M}_2 \\ \vdots \\ \mathbf{D}_p\mathbf{B}_p\mathbf{M}_p \end{bmatrix} \mathbf{x}_0 \qquad (4)$$

where $\mathbf{x}_0$ represents the common HR background image. We can then simplify (3) as

$$\begin{bmatrix} \mathbf{y}_1 \\ \mathbf{y}_2 \\ \vdots \\ \mathbf{y}_p \end{bmatrix} = \begin{bmatrix} \mathbf{D}_1\mathbf{B}_1\mathbf{M}_1 & \mathbf{D}_1\mathbf{B}_1 & 0 & \cdots & 0 \\ \mathbf{D}_2\mathbf{B}_2\mathbf{M}_2 & 0 & \mathbf{D}_2\mathbf{B}_2 & \vdots & \vdots \\ \vdots & \vdots & \cdots & \ddots & \vdots \\ \mathbf{D}_p\mathbf{B}_p\mathbf{M}_p & 0 & \cdots & \cdots & \mathbf{D}_p\mathbf{B}_p \end{bmatrix}$$
$$\times \begin{bmatrix} \mathbf{x}_0 \\ \mathbf{x}_1 \\ \vdots \\ \mathbf{x}_p \end{bmatrix} + \begin{bmatrix} \mathbf{n}_1 \\ \mathbf{n}_2 \\ \vdots \\ \mathbf{n}_p \end{bmatrix} \qquad (5)$$

By extending this single-band multiangle observation model to the multiangle multi/hyperspectral case, we can obtain the following model, with the assumption that the warping and

blurring for each band are the same:

$$\begin{bmatrix} \mathbf{y}_{11} & \cdots & \mathbf{y}_{1q} \\ \mathbf{y}_{21} & \cdots & \mathbf{y}_{2q} \\ \vdots & \vdots & \vdots \\ \mathbf{y}_{p1} & \cdots & \mathbf{y}_{pq} \end{bmatrix}$$
$$= \begin{bmatrix} \mathbf{D}_1\mathbf{B}_1\mathbf{M}_1 & \mathbf{D}_1\mathbf{B}_1 & 0 & \cdots & 0 \\ \mathbf{D}_2\mathbf{B}_2\mathbf{M}_2 & 0 & \mathbf{D}_2\mathbf{B}_2 & \vdots & \vdots \\ \vdots & \vdots & \cdots & \ddots & \vdots \\ \mathbf{D}_p\mathbf{B}_p\mathbf{M}_p & 0 & \cdots & \cdots & \mathbf{D}_p\mathbf{B}_p \end{bmatrix}$$
$$\times \begin{bmatrix} \mathbf{x}_{01} & \cdots & \mathbf{x}_{0q} \\ \mathbf{x}_{11} & \cdots & \mathbf{x}_{1q} \\ \vdots & \vdots & \vdots \\ \mathbf{x}_{p1} & \cdots & \mathbf{x}_{pq} \end{bmatrix} + \begin{bmatrix} \mathbf{n}_{11} & \cdots & \mathbf{n}_{1q} \\ \mathbf{n}_{21} & \cdots & \mathbf{n}_{2q} \\ \vdots & \vdots & \vdots \\ \mathbf{n}_{p1} & \cdots & \mathbf{n}_{pq} \end{bmatrix} \qquad (6)$$

where $q$ is the number of spectral bands of each angle image. Assuming that the downsampling matrix $\mathbf{D}_k$ and the blurring matrix $\mathbf{B}_k$ are the same for all the multiangle LR images, then the matrices $\mathbf{D}_k$ and $\mathbf{B}_k$ are substituted by $\mathbf{D}$ and $\mathbf{B}$. We can thus denote (6) as

$$\mathbf{Y} = \mathbf{A}\left(\boldsymbol{\theta}\right)\mathbf{X} + \mathbf{N} \qquad (7)$$

where $\mathbf{A}(\boldsymbol{\theta})$ denotes the degradation matrix for the background and foreground images, and $\boldsymbol{\theta}$ represents the image registration transformation parameters of matrix $\mathbf{M} = [\mathbf{M}_1\ \mathbf{M}_2 \ldots \mathbf{M}_p]^{\mathrm{T}}$. Homography transformation is used to describe the multiangle image registration transformation.

## B. Image Registration and Reconstruction Cost Function

Based on the observation model described above, our objective is to find a set of image registration transformation parameters $\boldsymbol{\theta}^*$ and the super-resolved HR images $\mathbf{X}^*$. The procedure of finding the HR images is always an ill-posed inverse problem. Based on MAP theory, the problem we need to solve can be transformed into a minimization problem as follows [13], [40]:

$$\hat{\mathbf{X}}, \hat{\boldsymbol{\theta}} = \operatorname{argmin} \rho\left(\mathbf{A}\left(\boldsymbol{\theta}\right)\mathbf{X} - \mathbf{Y}\right) + \lambda_1 U\left(\mathbf{X}\right) + \lambda_2 U\left(\boldsymbol{\theta}\right) \quad (8)$$

where $\rho(\mathbf{A}(\boldsymbol{\theta})\mathbf{X} - \mathbf{Y})$ and $\lambda_1 U(\mathbf{X}) + \lambda_2 U(\boldsymbol{\theta})$ are referred to as the data fidelity term and the regularization term about $\mathbf{X}$ and $\boldsymbol{\theta}$, respectively. $\lambda_1$ and $\lambda_2$ are the regularization parameters which balance these two terms.

The data fidelity term $\rho(\mathbf{A}(\boldsymbol{\theta})\mathbf{X} - \mathbf{Y})$ represents the similarity between the observed LR multiangle multi/hyperspectral images and the desired HR multi/hyperspectral images. This term is determined by the noise matrix in (6). If we assume that the noise present in the images is additive white Gaussian noise, then the Frobenius norm can be used to constrain the data fidelity term. The data fidelity term can then be represented by

$$\rho\left(\mathbf{A}\left(\boldsymbol{\theta}\right)\mathbf{X} - \mathbf{Y}\right) = \left\|\mathbf{A}\left(\boldsymbol{\theta}\right)\mathbf{X} - \mathbf{Y}\right\|_F \quad (9)$$

The prior information of the image registration transformation parameters is ignored here because of the very limited number of image registration transformation parameters. Therefore, only $U(\mathbf{X})$ is discussed here. In the traditional super-resolution MAP model, the TV regularization model is always utilized to regularize the ill-posed problem. The traditional way to extend the TV model to multi/hyperspectral images is by a band-by-band manner. This means that the TV model for each band is defined as a gray-level image TV model, and then the TV models of each band are added together, which indicates that the spectral correlation of the multi/hyperspectral remote sensing images is not considered. To consider the spectral correlation of the multi/hyperspectral remote sensing images, the MTV regularization model proposed by Blomgren and Chan [41] is utilized here to regularize the ill-posed problem. In addition, Yuan *et al.* [42] demonstrated that the MTV model has a powerful spectrally adaptive ability in remote sensing image processing. The MTV regularization model can be expressed as

$$U\left(\mathbf{X}\right) = \sum_{i=1}^{N_1 N_2} \sqrt{\sum_{j=1}^{q} \left|\nabla_{ij}\mathbf{X}\right|}$$

$$\nabla_{ij}\mathbf{X} = \sqrt{\left(\nabla_{ij}^h\mathbf{X}\right)^2 + \left(\nabla_{ij}^v\mathbf{X}\right)^2} \quad (10)$$

where $\nabla_{ij}^h\mathbf{X}$ and $\nabla_{ij}^v\mathbf{X}$ are linear operators corresponding to the horizontal and vertical first-order differences at the $i$th pixel and $j$th band, respectively. In this model, it is clear that all the bands are treated as an entirety, rather than as individual bands, which can exploit the spectral characteristics between bands more deeply. Substituting (9) and (10) into (8), we can obtain the following minimization cost function:

$$\hat{\mathbf{X}}, \hat{\boldsymbol{\theta}} = \operatorname{argmin}\left[\left\|\mathbf{A}\left(\boldsymbol{\theta}\right)\mathbf{X} - \mathbf{Y}\right\|_F\right.$$

$$\left. + \lambda \sum_{i=1}^{N_1 N_2} \sqrt{\sum_{j=1}^{q} \left|\nabla_{ij}\mathbf{X}\right|}\right] \quad (11)$$

According to the above-mentioned observation model (7), the UFRM for the joint super-resolution and registration of multiangle multi/hyperspectral images is established here, which includes two unknown parameters $\mathbf{X}$ and $\boldsymbol{\theta}$. The detailed optimization solution is given in the next subsection.

## C. Optimization

The optimization problem shown in (11) is nonconvex. The alternating algorithm for the minimization of a nonconvex function proposed by Attouch *et al.* [43] is utilized here. This algorithm iteratively estimates both the HR image $\mathbf{X}$ and the image registration transformation parameters $\boldsymbol{\theta}$ in a two-step optimization procedure. The main steps of this optimization algorithm can be stated as follows. The image registration parameters and the HR images are resolved in an alternating manner. A is the degradation matrix which contains D, B, and M (M is unknown), and $\mathbf{Y}$ is the LR observation images. The desired HR image $\mathbf{X}$ and image registration parameters $\boldsymbol{\theta}$, which are the parameters of M, can be updated by minimizing the following cost function:

$$L\left(\mathbf{X}, \boldsymbol{\theta}\right) = \left\|\mathbf{A}\left(\boldsymbol{\theta}\right)\mathbf{X} - \mathbf{Y}\right\|_F + \lambda U\left(\mathbf{X}\right) \quad (12)$$

*1) Updating the HR Images:* We let $(\mathbf{X}^k, \boldsymbol{\theta}^k)$ be the estimates obtained after $k$ iterations of the algorithm. Given the estimate of registration parameters $\boldsymbol{\theta}^k$, the HR images can be updated by minimizing the following equation:

$$\mathrm{E}_1\left(\mathbf{X}^{k+1}\right) =$$

$$\left\|\mathbf{A}\left(\boldsymbol{\theta}^k\right)\mathbf{X}^{k+1} - \mathbf{Y}\right\|_F + \lambda U\left(\mathbf{X}^{k+1}\right) + \frac{\lambda_{\mathrm{x}}}{2}g\left(\mathbf{X}^{k+1} - \mathbf{X}^k\right) \quad (13)$$

where $g$ acts as a proximal term and $\lambda_{\mathrm{x}} > 0$ as the step size. $g$ is a proper lower-semicontinuous convex function, such that $g(\mathrm{x}) \geq 0$ for all of $x$, and $g(0) = 0$. It is clear that this implies that

$$L\left(\mathbf{X}^{k+1}, \boldsymbol{\theta}^k\right) + \frac{\lambda_{\mathrm{x}}}{2}g\left(\mathbf{X}^{k+1} - \mathbf{X}^k\right) \leq L\left(\mathbf{X}^k, \boldsymbol{\theta}^k\right) \quad (14)$$

Hence $L(\mathbf{X}^{k+1}, \boldsymbol{\theta}^k) \leq L(\mathbf{X}^k, \boldsymbol{\theta}^k)$ with a decrease of $\lambda_{\mathrm{x}}g(\mathbf{X}^{k+1} - \mathbf{X}^k)/2$, at least.

*2) Updating the Registration Parameters:* We let $(\mathbf{X}^k, \boldsymbol{\theta}^k)$ be the estimates obtained after $k$ iterations of the algorithm, and $\mathbf{X}^{k+1}$ is the solution of (13). A projected Newton-like method [44] is used to update the transformation parameters. Given the estimate of HR image $\mathbf{X}^{k+1}$, the cost function to update the registration parameter can be given as

$$\mathrm{E}_2\left(\boldsymbol{\theta}^{k+1}\right) = \left\|\mathbf{A}\left(\boldsymbol{\theta}^{k+1}\right)\mathbf{X}^{k+1} - \mathbf{Y}\right\|_F$$

$$+ \lambda U\left(\mathbf{X}^{k+1}\right) + \frac{\lambda\lambda_{\theta}}{2}\left\|\boldsymbol{\theta}^{k+1} - \boldsymbol{\theta}^k\right\|_2^2 \quad (15)$$
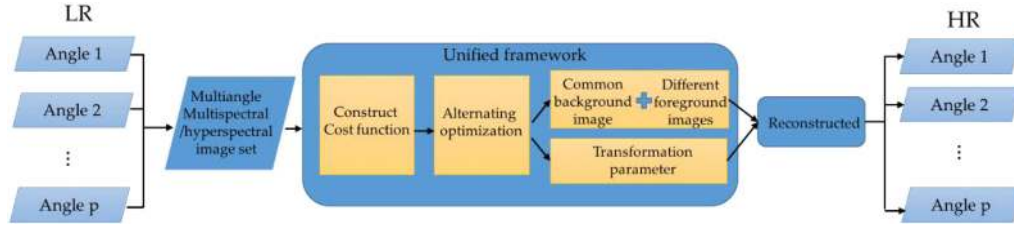
Fig. 2. Flowchart of the proposed UFRM algorithm.

---

**Algorithm 1:** Multiangle Multi/Hyperspectral Image Super-Resolution

**Input:** A data set of multiangle multi/hyperspectral LR images

**Step 1: Initialization:**

Vectorize all the multiangle multi/hyperspectral LR images and combine them to form multiangle multi/hyperspectral data set $\mathbf{Y}$.

**Step 2: Construct the cost function:**

Perform $\mathbf{X}, \boldsymbol{\theta}$ estimation with the $\mathbf{Y}$ matrix in (11) to construct the cost function:

$L(\mathbf{X}, \boldsymbol{\theta}) = \|\mathbf{A}(\boldsymbol{\theta})\mathbf{X} - \mathbf{Y}\|_F + \lambda U(\mathbf{X})$.

**Step 3: Solve the cost function**

The alternating minimization strategy is utilized to solve the cost function.

   1) Set $k = 0$, $\mathbf{X}^0 = 0$, and $\boldsymbol{\theta}^0 = 0$; $k_{max}$ and $\lambda$, $\lambda_{\mathbf{x}}$, $\lambda_{\theta}$

   2) While not convergence and $k \leq k_{max}$:

     a. Optimize $\mathbf{X}^{k+1}$ while fixing $\boldsymbol{\theta}^k$

$\mathrm{E}_1(\mathbf{X}^{k+1}) = \|\mathbf{A}(\boldsymbol{\theta}^k)\mathbf{X}^{k+1} - \mathbf{Y}\|_F + \lambda U(\mathbf{X}^{k+1}) + \frac{\lambda_{\mathbf{x}}}{2} g(\mathbf{X}^{k+1} - \mathbf{X}^k)$,

     b. Optimize $\boldsymbol{\theta}^{k+1}$, keeping $\mathbf{X}^{k+1}$ fixed from

$\mathrm{E}_2(\boldsymbol{\theta}^{k+1}) = \|\mathbf{A}(\boldsymbol{\theta}^{k+1})\mathbf{X}^{k+1} - \mathbf{Y}\|_F + \lambda U(\mathbf{X}^{k+1}) + \frac{\lambda\lambda_{\theta}}{2}\|\boldsymbol{\theta}^{k+1} - \boldsymbol{\theta}^k\|_2^2$,

     c. $\mathrm{k} \leftarrow \mathrm{k} + 1$

Simultaneously obtain the transformation parameters $\boldsymbol{\theta}^*$ and matrix $\mathbf{X}^*$.

**Step 4: Reconstruct the HR images**

Obtain all the reconstructed images for every angle according to $\boldsymbol{\theta}^*$ and $\mathbf{X}^*$:

$\mathbf{x}_{nm} = \mathbf{M}_n \mathbf{x}_{0m}^* + \mathbf{x}_{nm}^*$,

**Output:** Super-resolved image $\mathbf{X}$.

---

According to the algorithm in [31], the inequalities of $\boldsymbol{\theta}$ can be obtained as

$$L\left(\mathbf{X}^{k+1}, \boldsymbol{\theta}^{k+1}\right) + \frac{\lambda\lambda_{\theta}}{2}\left\|\boldsymbol{\theta}^{k+1} - \boldsymbol{\theta}^k\right\|_2^2 \leq L\left(\mathbf{X}^{k+1}, \boldsymbol{\theta}^k\right) \tag{16}$$

where $\lambda_{\theta}$ is the step size. Therefore, $L(\mathbf{X}^{k+1}, \boldsymbol{\theta}^{k+1}) \leq L(\mathbf{X}^{k+1}, \boldsymbol{\theta}^k)$ with a decrease of $\lambda_{\theta}\boldsymbol{\theta}^{k+1} - \boldsymbol{\theta}^{k^2}{}_2/2$, at least. Differing from the traditional two-stage SRR methods that perform the image registration on the LR images in the first stage, the image registration is performed iteratively. It is believed that this cyclic optimization procedure can prevent the effect of image registration errors to some extent.

*3) Reconstructing the HR Images:* After we obtain the estimated images $\mathbf{X}^*$ and transformation parameters $\boldsymbol{\theta}^*$, the reconstructed images can be obtained by

$$\mathbf{x}_{nm} = \mathbf{M}_n \mathbf{x}_{0m}^* + \mathbf{x}_{nm}^* \tag{17}$$

where $\mathbf{x}_{0m}^*$ and $\mathbf{x}_{nm}^*$ are the estimated background image and foreground image in the $m$th band and $n$th angle.

*4) Procedure Flow:* The overall procedure flow of SRR for multiangle multi/hyperspectral images can be summarized as shown in Algorithm 1. The flowchart of the proposed UFRM algorithm is also presented in Fig. 2. The Angle 1 to Angle $p$ means the input multi/hyperspectral images at different angles. These images are vectorized and stacked to form a 2-D data set $\mathbf{Y}$. The cost function is then constructed, and an alternating optimization strategy is utilized to obtain the transformation parameters $\boldsymbol{\theta}^*$ and matrix $\mathbf{X}^*$. $\mathbf{X}^*$ is composed of the common background image and different foreground images. Finally, the super-resolved image $\mathbf{X}$ is reconstructed by (17).

## III. EXPERIMENTS

### A. Experimental Setting

Two sources of data were used in the experiments. WorldView-2 and CHRIS/PROBA images were chosen to represent multiangle multispectral and hyperspectral images, respectively. The WorldView-2 images, which were provided by DigitalGlobe, cover Santos Dumont Airport of Rio de Janeiro, Brazil. The latitude of the WorldView-2 images ranges from $22°54'07.7''$S to $22°55'11.9''$S, and the longitude ranges from $43°10'38.8''$W to $43°09'27.8''$W. The CHRIS/PROBA images cover the urban area of London, Ontario, Canada. The latitude of the CHRIS/PROBA images is between $42°54'44.1''$N and $43°04'04.3''$N, and the longitude is between $81°05'31.4''$W and $81°21'43.0''$W. WorldView-2 provides five angular images $(+45.3°, +34°, +8.6°, -30.2°, \text{and} -45.4°$, where the smaller the angle, the closer the image is to the nadir image), each of which contains an eight-band multispectral image with a spatial resolution of 1.8 m [45]. The five different angle multispectral images are shown in Fig. 3. The CHRIS/PROBA system also provides multiple observations of the same scene at five different angles $(+55°, +36°, 0°, -36°, \text{and} -55°$, where the smaller the angle, the closer the image is to the nadir image) [46]. Each angle image contains an 18-band hyperspectral image with a spatial resolution of 17 m. According to Galbraith *et al.* [36], symmetric view angle images and images closer to the nadir
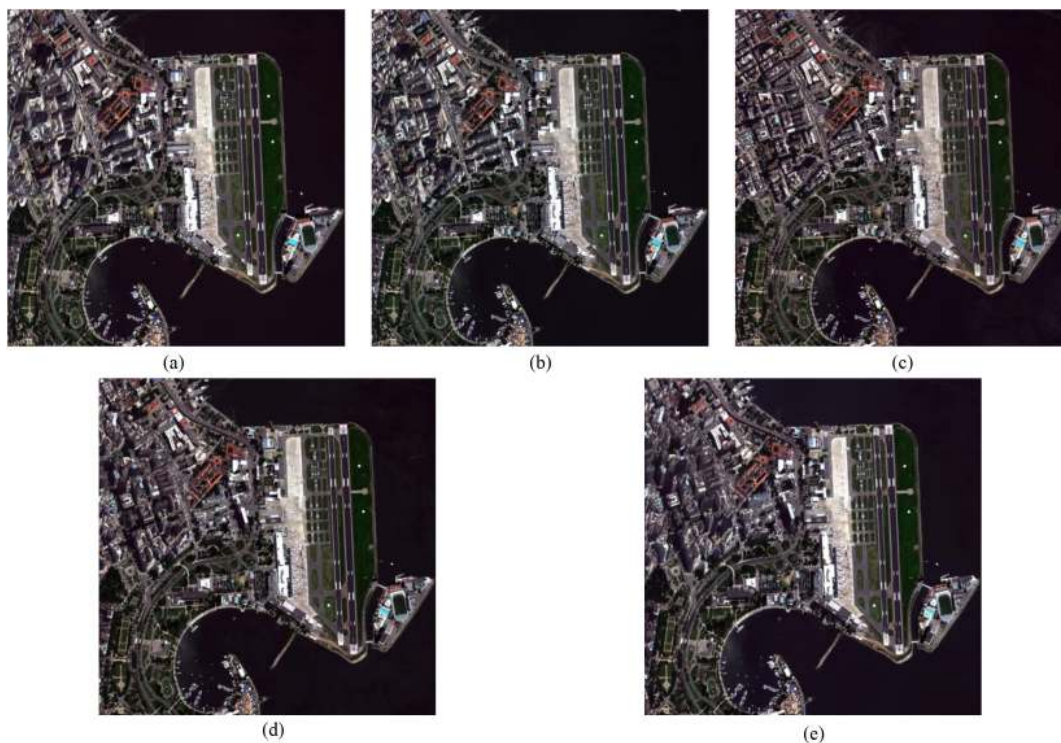
Fig. 3. Five WorldView-2 different angle images. (a)–(e) Fly-by zenith angles are $+45.3°$, $+34°$, $+8.6°$ (which is the most nadir one), $-30.2°$, and $-45.4°$, respectively.
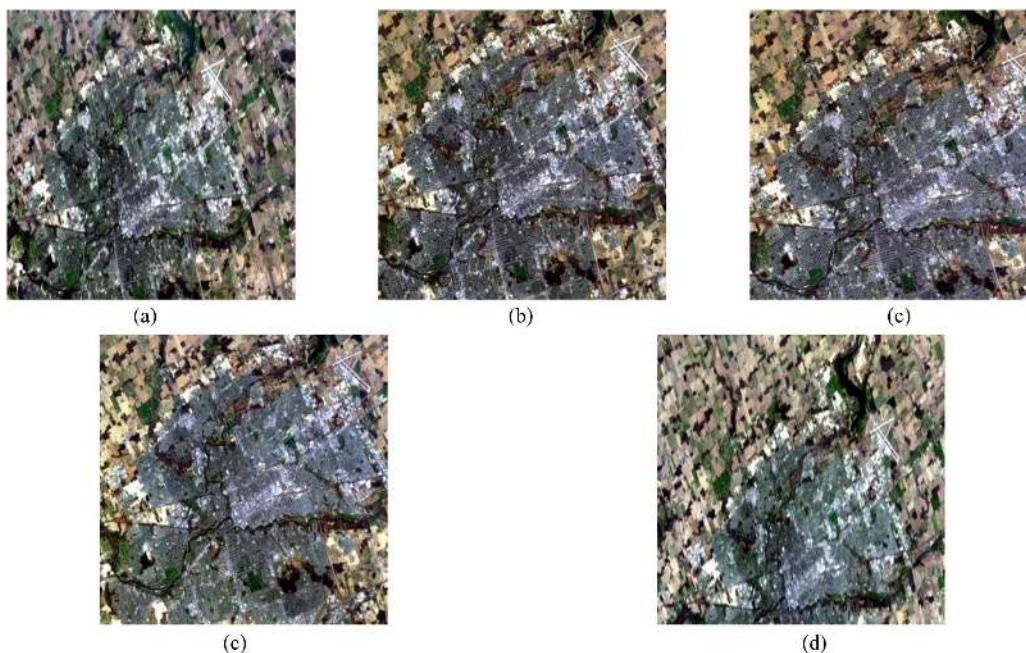


Fig. 4. Five CHRIS/PROBA different angle images. (a)–(e) Fly-by zenith angles are $+55°$, $+36°$, $0°$(which is the most nadir one), $-36°$, and $-55°$, respectively.

image are more suitable for resolution enhancement. However, using views of more than $48°$ off-nadir is counterproductive for resolution enhancement. Therefore, two symmetric images and the nadir image were used in the CHRIS/PROBA data set. In addition, the two CHRIS/PROBA images of $55°$ and $-55°$

with serious distortion were removed from the data set. The five different angle hyperspectral images are shown in Fig. 4. Three simulation data sets were used in the experiments. Data set 1 and Data set 2 are subregion images of the WorldView 2 images, and Data set 3 is a subregion of the CHRIS/PROBA images. Detailed

descriptions of the three simulation data sets are provided in the following.

In the simulation experiments, the peak signal-to-noise ratio (PSNR) and the structural similarity index (SSIM) were used to evaluate the quality of the reconstruction image. The mean PSNR (MPSNR) and mean SSIM (MSSIM) were also used to measure the quality of the reconstruction image for all the bands. Furthermore, the spectral angle mapper (SAM) index was also applied to measure the spectral distortion.

The PSNR is widely used in the quality assessment of image super-resolution, and is based on the mean-square error between the reference image and reconstruction image, which is related to the logarithm of $(2^n - 1)^2$, where $n$ is the number of bits for each pixel value. We generally use eight bits to represent each pixel, so the formulation can be represented as

$$\text{PSNR} = 10\log_{10} \frac{255^2 \times MN}{\sum_{i=1}^{MN} \left( \hat{\mathbf{X}}_i - \mathbf{X}_i \right)^2} \qquad (18)$$

where $\mathbf{X}_i$ stands for the gray value of the reference image, and $\hat{\mathbf{X}}_i$ represents the gray value of the SRR image in the corresponding location to the reference image. $MN$ is the image size. A better result will have a higher PSNR value. The PSNR value can assess the quality of the reconstruction result to a certain degree. The MPSNR is the mean value of all the image bands, and is defined as

$$\text{MPSNR} \left( \mathbf{X}, \hat{\mathbf{X}} \right) = \frac{1}{M} \sum_{j=1}^{M} \text{PSNR} \left( \mathbf{X}_j, \widehat{\mathbf{X}_j} \right) \qquad (19)$$

where $\mathbf{X}$ and $\hat{\mathbf{X}}$ stand for all the bands of the reference images and the reconstruction images. $M$ is the total number of bands, and $j$ represents the band that is calculated.

The SSIM, which was proposed by Wang et al. [47], has been widely used for the evaluation of the quality of reconstructed images. The SSIM represents the image contrast, image brightness, and structural similarity. A larger SSIM value means a better image reconstruction quality. The SSIM formulation can be described as

$$\text{SSIM} = \frac{\left( 2\mu_{\mathbf{X}}\mu_{\hat{\mathbf{X}}} + C_1 \right) \left( 2\sigma_{\mathbf{X}\hat{\mathbf{X}}} + C_2 \right)}{\left( \mu_{\mathbf{X}}^2 + \mu_{\hat{\mathbf{X}}}^2 + C_1 \right) \left( \sigma_{\mathbf{X}}^2 + \sigma_{\hat{\mathbf{X}}}^2 + C_2 \right)} \qquad (20)$$

where $\mu_X$ and $\mu_{\hat{X}}$ stand for the average value of the reference image and reconstruction image. $\sigma_X$ and $\sigma_{\hat{X}}$ represent their variance. $\sigma_{X\hat{X}}$ is the covariance of the reference image and reconstruction image. $C_1$ and $C_2$ are both constant values to prevent the equation from being meaningless. In the simulation experiments, we set the constants $C_1$ and $C_2$ to 0.01 and 0.03, respectively. We used the MSSIM index to evaluate the overall image quality, which can be described as

$$\text{MSSIM} \left( \mathbf{X}, \hat{\mathbf{X}} \right) = \frac{1}{M} \sum_{j=1}^{M} \text{SSIM} \left( \mathbf{X}_j, \widehat{\mathbf{X}_j} \right) \qquad (21)$$

where the meanings of $\mathbf{X}$, $\hat{\mathbf{X}}$, $M$, and $j$ are the same as those in MPSNR.

The SAM [48] is an index that measures the spectral similarity between the reconstruction image spectra and the reference spectra. A small angle between the two spectra means a high similarity between target image and reference image. The formulation can be described as

$$\text{SAM} \left( \mathbf{X}, \hat{\mathbf{X}} \right) = \arccos \left( \frac{\mathbf{X}, \hat{\mathbf{X}}}{\|\mathbf{X}\|_2 \cdot \left\| \hat{\mathbf{X}} \right\|_2} \right) \qquad (22)$$

where $\mathbf{X}$ and $\hat{\mathbf{X}}$ are the two spectral vectors. $\mathbf{X}$ is the original spectral pixel vector, and $\hat{\mathbf{X}}$ is the distorted vector obtained by applying super-resolution to the coarser remote sensing data.

In the real-data experiments, the cumulative probability of blur detection (CPBD) was used to measure the reconstruction results. The CPBD, which was proposed by Narvekar et al. [49], is mainly used to measure image sharpness. The main principle of CPBD is expressed as

$$\text{P}_{\text{BLUR}} = P(e_i) = 1 - \exp \left( -\left| \frac{w(e_i)}{w_{\text{JNB}}(e_i)} \right|^{\beta} \right) \qquad (23)$$

$$\text{CPBD} = \text{P}\left(\text{P}_{\text{BLUR}} \leq \text{P}_{\text{JNB}}\right) = \sum_{\text{P}_{\text{BLUR}}=0}^{\text{P}_{\text{BLUR}} \leq \text{P}_{\text{JNB}}} \text{P}\left(\text{P}_{\text{BLUR}}\right) \qquad (24)$$

where $\text{P}_{\text{BLUR}}$ represents the probability of blur detection. $w_{\text{JNB}}(e_i)$ is "just noticeable" blur (JNB). $w(e_i)$ denotes the measured width of edge $e_i$. $\text{P}(\text{P}_{\text{BLUR}})$ represents the probability distribution function (PDF) value when $\text{P}_{\text{BLUR}}$ is known. The CPBD value is between 0 to 1, and a high CPBD value means a better result.

To show the effectiveness of the proposed UFRM method, we used the angular difference weighted super-resolution (AWSR) method [21] and the multiangle super-resolution method tested on ZY-3 three line camera (TLC) images proposed in [33] as comparative methods. The procedures of image registration and SRR in the AWSR and TLC methods are separate. The method proposed by Gilles Puy (GP) [38] was also used in the comparison. The GP method can simultaneously achieve image registration and SRR, but it does not consider the high correlation between the different bands of each angle image. The traditional bilinear method was also used as a comparative method.

### B. Simulation Experiments

*1) Multiangle Multispectral Image Data Sets:* Data set 1 and Data set 2 are subregion images of WorldView-2 images, made up of airport areas sized $128 \times 128$ and $64 \times 64$, respectively. The images of both Data sets 1 and 2 were downsampled to half size in the vertical and horizontal directions. The downsampled images were then super-resolved and the SRR results were compared with the original HR images. The reconstruction factor in both the vertical and horizontal directions was set as 2. The regularization parameter $\lambda$ was chosen through a sequence of experiments. The nadir or close-nadir images are the most widely used in remote sensing applications, so the nadir or close-nadir images of the original HR multi/hyperspectral
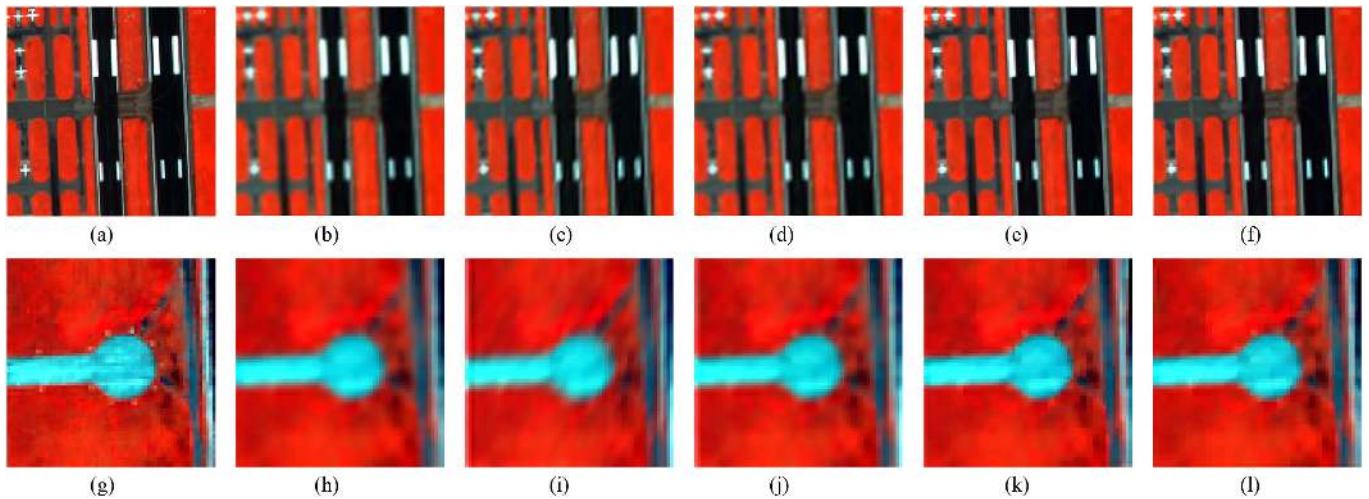
Fig. 5.    Super-resolution results obtained with the Data set 1 and Data set 2 images. (a) and (g) Reference images for Data set 1 and Data set 2, respectively. (b) Bilinear. (c) AWSR. (d)TLC. (e) GP. (f) UFRM. (h) to (l) Results of methods (b)–(l) utilized on Data set 2.

TABLE I
QUANTITATIVE EVALUATION OF THE DIFFERENT SUPER-RESOLUTION METHODS WITH THE SIMULATION DATA SETS

| Method | | Bilinear | AWSR | TLC | GP | Proposed UFRM method |
|---|---|---|---|---|---|---|
| | MPSNR | 21.4298 | 26.6626 | 24.5821 | <u>28.6536</u> | **28.9110** |
| Data set 1 | MSSIM | 0.9569 | <u>0.9864</u> | 0.9739 | 0.9863 | **0.9871** |
| | SAM | 3.0687 | 3.6751 | 4.0225 | <u>2.7349</u> | **2.6888** |
| | MPSNR | 25.9575 | 23.8160 | 26.4532 | <u>27.2528</u> | **28.8749** |
| Data set 2 | MSSIM | 0.9873 | 0.9890 | 0.9882 | <u>0.9925</u> | **0.9928** |
| | SAM | 1.9872 | 2.9648 | 1.9785 | <u>1.8620</u> | **1.7237** |
| | MPSNR | 25.8063 | 28.6279 | 25.9741 | <u>28.9014</u> | **29.6001** |
| Data set 3 | MSSIM | 0.9858 | 0.9906 | 0.9862 | <u>0.9907</u> | **0.9915** |
| | SAM | 3.0861 | 3.1475 | 3.4674 | <u>3.1174</u> | **3.0387** |

images were chosen as the reference for the qualitative and quantitative analyses. For the bilinear method, an interpolation operation was applied to the images. For the AWSR and TLC methods, the images were first registered, and SRR was then applied to the registered images. The GP method does not require image registration before SRR. The SRR results obtained with Data set 1 and Data set 2 are shown in Fig. 5. To enhance the contrast between the different methods, the eighth, third, and second band images were combined as the false-color images.

From Fig. 5(b)–(f), it can be clearly observed that the GP method and the proposed UFRM method can achieve better results than the other methods. The details of the images are well reconstructed by the UFRM method and GP method, especially in the boundary area of the road and the lawn in Fig. 5(f). In Fig. 5(l), the fine details of the circular part are well reconstructed by the proposed UFRM method. The reconstruction result of the AWSR method is not as sharp as the result of the UFRM method. It can also be observed that there are some artifacts in the reconstruction result of the AWSR method, which are caused by the poor transformation estimation. As the TLC method does

not have spatial and spectral constraints in the super-resolution model, the super-resolution result of the TLC method is poor.

The quantitative evaluation results are shown in Fig. 6 and listed in Table I. From Fig. 6, it can be seen that the PSNR and SSIM values of the proposed UFRM method are the best in almost all the bands, and the GP method achieves the best results in one or two bands of the multi/hyperspectral images. As the UFRM method considers the high correlation between the different bands, the reconstruction result of the UFRM method is more stable. Table I presents the MPSNR, MSSIM, and SAM values of the five SRR approaches. The best evaluation result for the whole image is marked in bold, and the second-best result is underlined. For the other four super-resolution methods, as the spectral information constraint is not considered in the super-resolution process, they all show more serious spectral distortion than the UFRM method (from the SAM values). In terms of all three quantitative evaluation indices, the proposed UFRM method obtains better results than the other methods. Overall, it can be concluded that the proposed UFRM method achieves the best SRR performance.
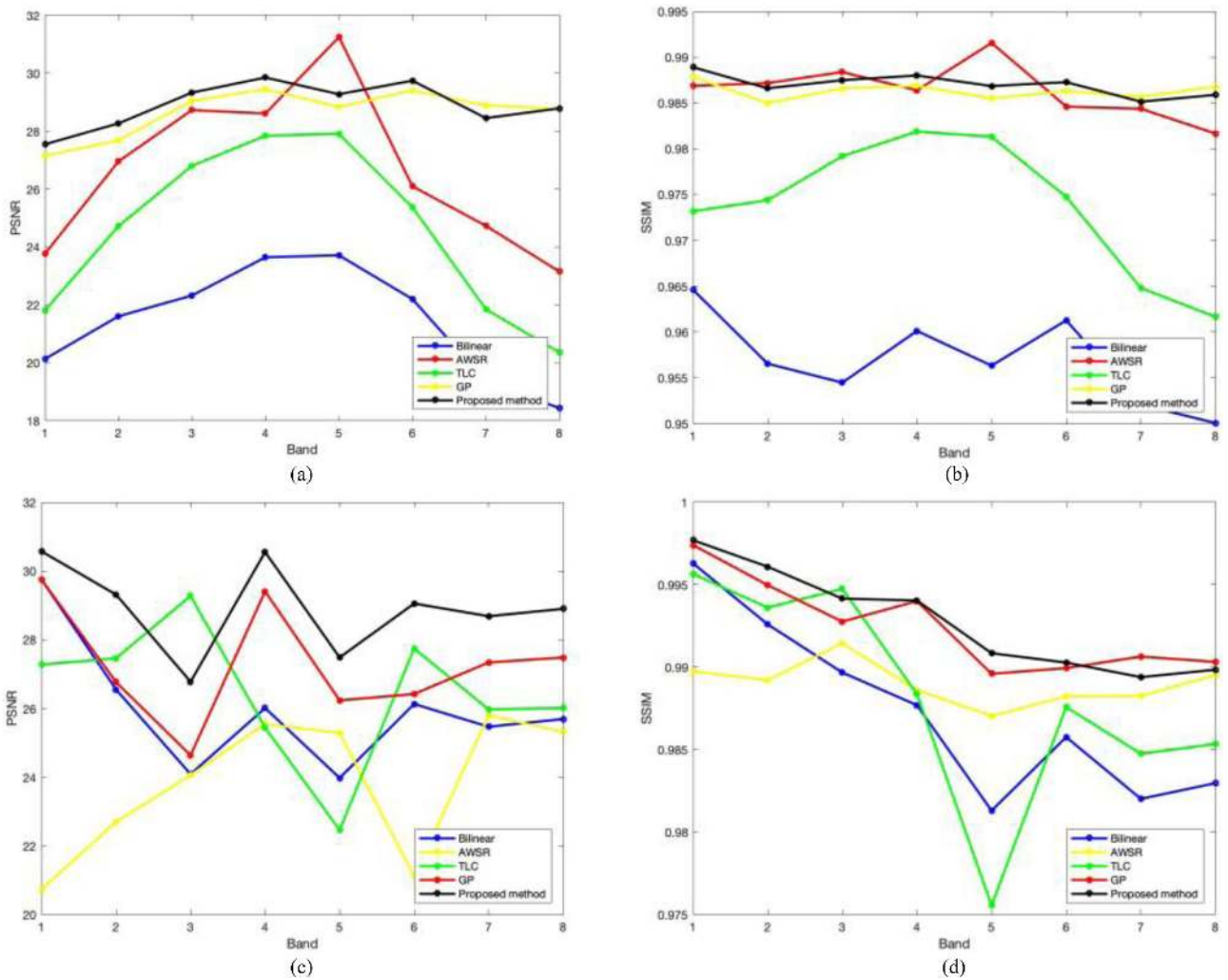
Fig. 6. PSNR and SSIM values of the different bands of Data set 1 and Data set 2. (a) PSNR of Data set 1. (b) SSIM of Data set 1. (c) PSNR of Data set 2. (d) SSIM of Data set 2.
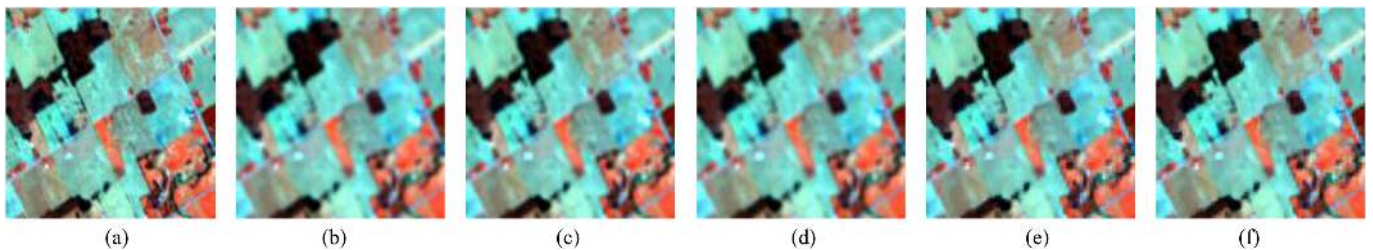


Fig. 7. Super-resolution results obtained with Data set 3. (a) Reference image. (b) Bilinear. (c) AWSR. (d)TLC. (e) GP. (f) UFRM.

*2) Multiangle Hyperspectral Image Data Set:* Data Set 3 sized $64 \times 64$ is a subregion of a farm area cropped from the CHRIS/PROBA images shown in Fig. 4. The method of operation for Data set 3 was the same as the method for Data set 1 and Data set 2. The SRR results of the five different methods are shown in Fig. 7. The 18th, 5th, and 1st band images were combined as the false-color images for visualization. A visual inspection of the reconstruction results of the proposed UFRM

method and GP method suggests that these methods perform better than the other methods. In the reconstruction results of the AWSR and TLC methods, the images are blurred to some extent. It can be observed that the reconstruction results of the AWSR and TLC methods show blurring in Fig. 7(c)–(d), whereas the proposed UFRM method can reconstruct the detailed informa-tion well. The quantitative evaluation is provided in Fig. 8 and Table I. The SAM values of Data set 3 listed in Table I confirm
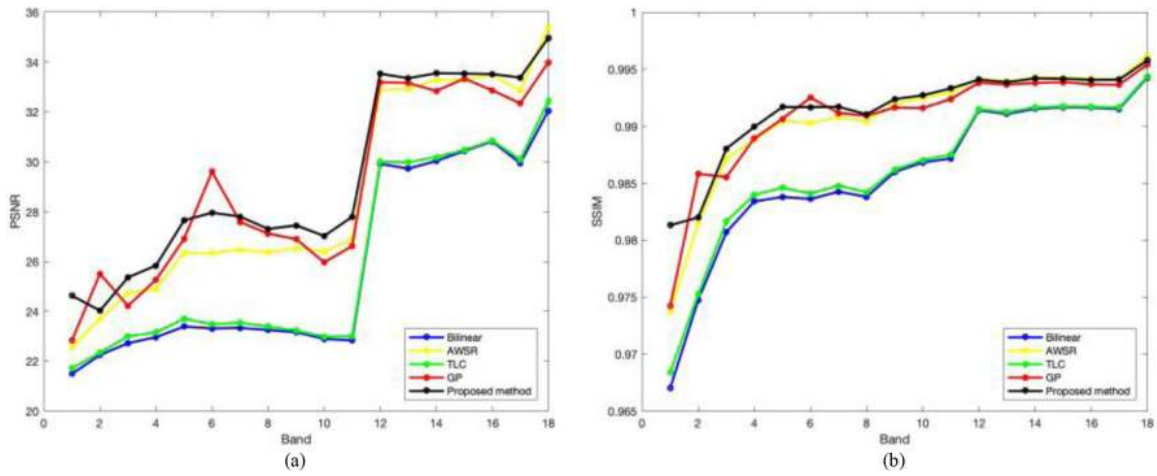
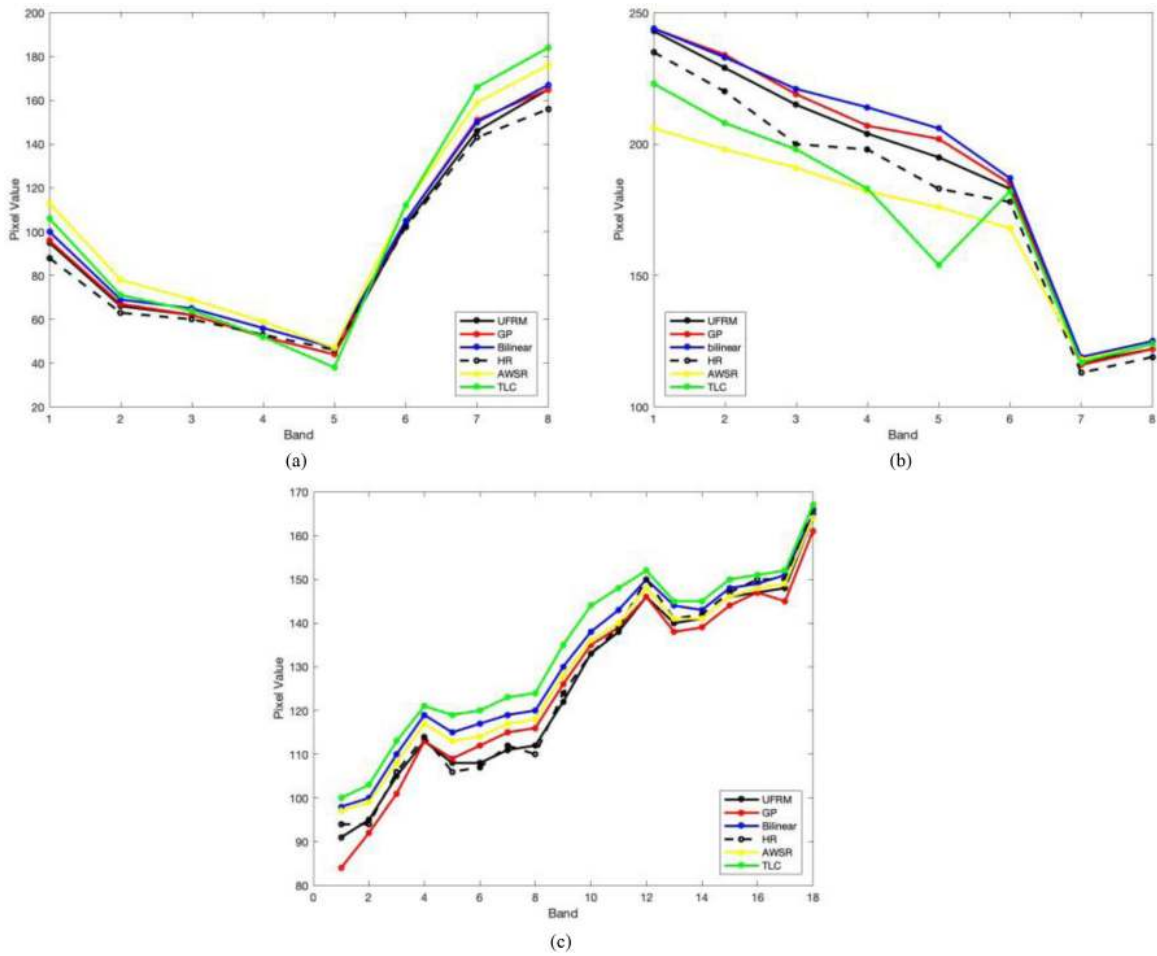Fig. 8.    PSNR and SSIM values of the different bands of Data set 3. (a) PSNR. (b) SSIM.



Fig. 9.    Spectra of the reconstruction results obtained using the different methods on the simulation data. (a) WorldView-2 Data set 1. (b) WorldView-2 Data set 2. (c) CHRIS/PROBA Data set 3.
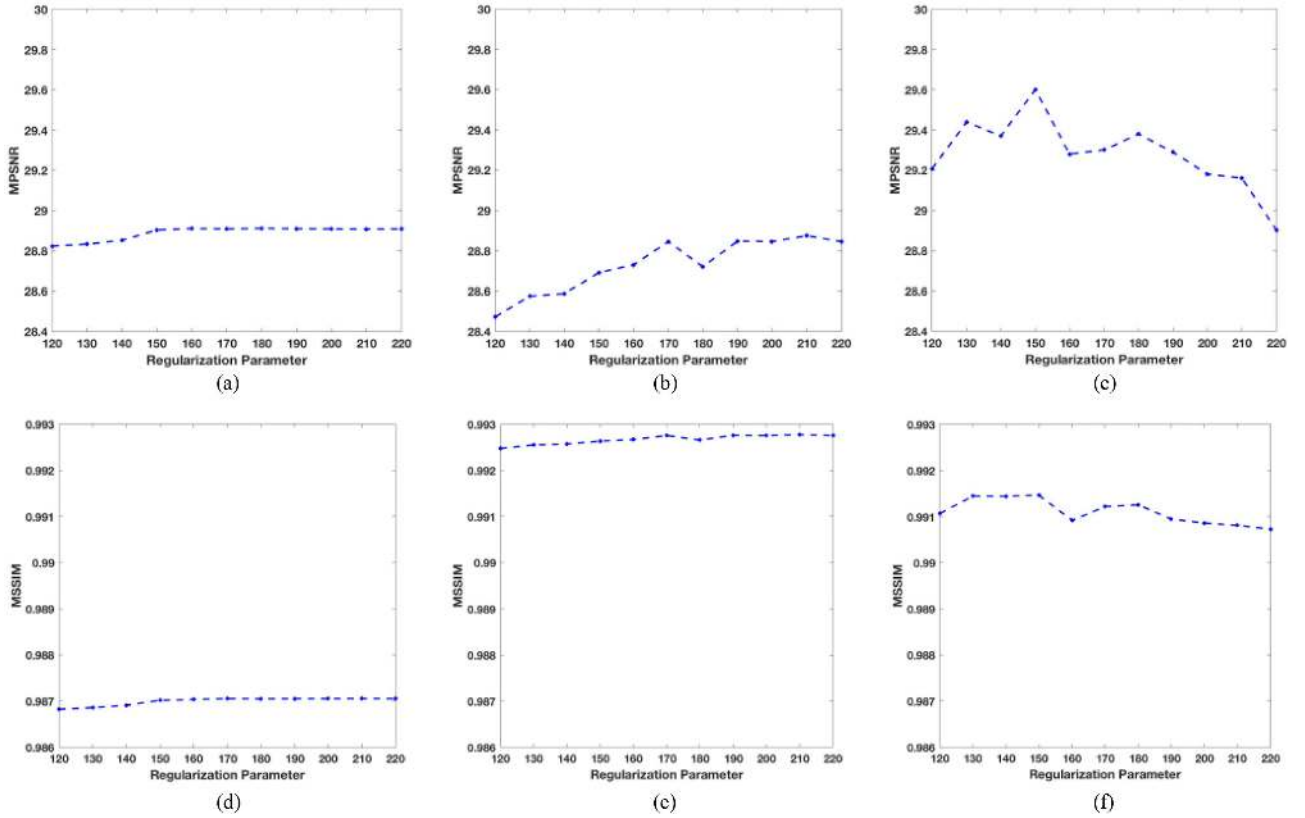
Fig. 10.    MPSNR and MSSIM values for different regularization parameters in Data sets 1–3. (a) and (d) Data set 1. (b) and (e) Data set 2. (c) and (f) Data set 3.

that the UFRM method can maintain the spectral information well. The MPSNR and MSSIM values illustrate the effectiveness of the proposed UFRM method. From both the qualitative and quantitative evaluations, the proposed UFRM method obtains the best results. The proposed UFRM method also shows a stable reconstruction performance in both the multispectral case and hyperspectral case.

*3) Analysis of the Algorithm Performance in the Spectral Domain:* To further compare the performances of the different algorithms in the spectral domain, spectral signatures are shown in Fig. 9. Fig. 9(a) shows the spectral signatures for pixel (50,50) in Data set 1; Fig. 9(b) shows the spectral signatures of pixel (28,40) in Data set 2; and Fig. 9(c) shows the spectral signatures of pixel (60,70) in Data set 3. From Fig. 9, it can be observed that the proposed UFRM method produces better spectral signatures than the other methods when compared with the HR spectrum. The proposed UFRM method, which is represented by the black solid lines, is always the closest to the HR spectrum, which is represented by the black dotted lines. From both the SAM values listed in Table I and the spectral curves shown in Fig. 9, the proposed UFRM method shows the best performance in maintaining spectral information.

*4) Sensitivity Analysis of Parameter λ:* In the UFRM model, λ is the parameter used to trade off the regularization term. To acquire the optimal value of the regularization parameter, we conducted a series of experiments on the different data sets used in the simulation experiments. Fig. 10 shows the sensitivity of

the MPSNR and MSSIM to the regularization parameter λ. As shown in Fig. 10, the horizontal axis represents the value of the regularization parameter, and the vertical axis shows the quantitative evaluation factor. According to this analysis, the value of λ should be selected when λ tends to be stable and obtains relatively high MPSNR and MSSIM values. Generally speaking, the super-resolution result of the proposed UFRM method is quite stable and robust to the variation of regularization parameter λ.

*5) Analysis of the Reconstruction Error Map:* In order to show the performance of the proposed UFRM method compared with the GP method, the reconstruction error maps for the GP method and the proposed method are presented in Fig. 11. The error maps were obtained by $\epsilon = (I_{\mathrm{reconstucted}} - I_{\mathrm{ref}})^2/I_{\mathrm{ref}}$. Fig. 11(a)–(c) shows the error maps obtained using the GP method for the three simulation data sets, and Fig. 11(d)–(f) shows the error maps obtained with the proposed method. It is clear that the proposed method shows a good performance, especially on Data set 2 and Data set 3. The reconstruction performance on flat areas is more uniform when using the UFRM method, which can be seen in Fig. 11(e)–(f). In addition, the boundaries in Data set 2 and Data set 3 can be reconstructed well using the proposed method.

*6) Analysis of the Time Consumption and Computational Complexity:* The time consumption of the five methods in the simulation experiments is presented in Table II. All the experiments were carried out on a Mac OS system, with the main
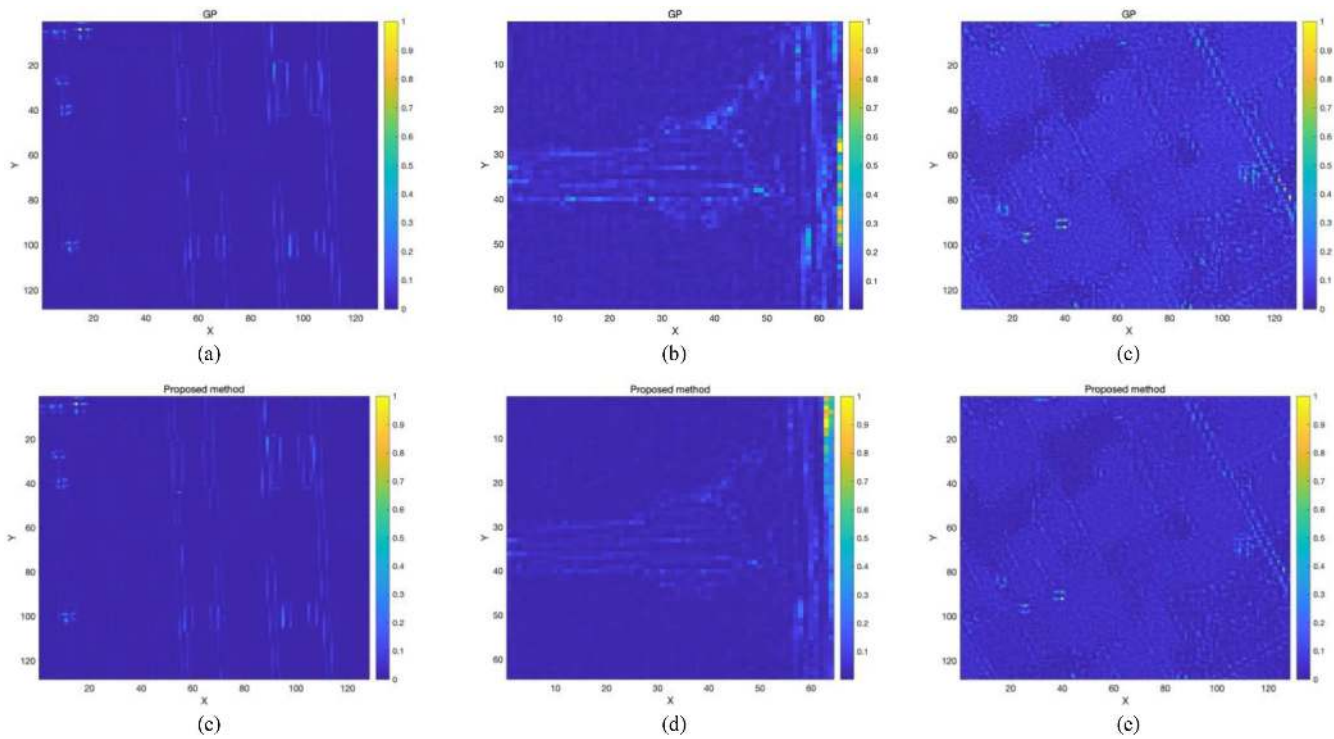
Fig. 11.    Error maps for the three simulation datasets using the GP method and the proposed UFRM method.

TABLE II
TIME CONSUMPTION OF THE DIFFERENT METHODS WITH THE DIFFERENT SIMULATION DATA SETS

| | Method | Bilinear | AWSR | TLC | GP | Proposed UFRM method |
|---|---|---|---|---|---|---|
| Time (seconds) | Data set 1 | 0.7 | 39.3 | 90.9 | 3838.4 | 3878.8 |
| | Data set 2 | 0.4 | 6.2 | 17.9 | 954.5 | 753.0 |
| | Data set 3 | 1.2 | 75.3 | 137.5 | 18363.1 | 6265.8 |

frequency of the CPU being 3.1 GHz. It can be observed that the time consumption of the bilinear method, AWSR method, and TLC method is low, but the reconstruction results of these methods are relatively poor. Compared with the GP method, the proposed method still shows superiority in time efficiency. Although the proposed method is relatively slow, it does obtain the best results. In addition, with the ongoing development of computer technology, we believe that the time consumption will not be a major problem for much longer.

The computational complexity analysis for the proposed algorithm is as follows. Suppose that the angle number of the multi/hyperspectral images is $p$ and the band number is $q$, the size of a single-band image of the input data is $H \times L$, and $w$ is the number of registration parameters. According to the algorithm proposed in [38], a $t_1$ times iterative descent optimization procedure is utilized, which occupies most of the computational load when updating the HR image section. The computational complexity of this procedure is $O(pq(H \times L \times H))$ in each iteration step. In the updating of the registration parameter procedure, a $t_2$ times iterative descent optimization procedure is utilized, for which the computational

complexity is $O(wpq(H \times L \times H))$ in each iteration step. The whole computational complexity in each iteration step is then $t_1 O(pq(H \times L \times H)) + t_2 O(wpq(H \times L \times H))$. If $H$ is equal to $L$, then the computational complexity becomes $t_1 O(pqH^3) + t_2 O(wpqH^3)$ in each iteration step.

### C. Real-Data Experiments

The effectiveness of the proposed method was also tested in real-data experiments. The WorldView-2 images and CHRIS/PROBA images were again used in the real-data experiments. Real data set 1 is a subregion of the WorldView-2 images, which contains an airport area sized $64 \times 64$. Real data set 2 is an airport subregion of the CHRIS/PROBA images sized $64 \times 64$.

The reconstruction factor in both the vertical and horizontal directions was set to 2. The bilinear method, AWSR method, TLC method, and GP method were used as benchmark methods. The reconstruction procedure was directly conducted for the multiangle multi/hyperspectral images in the same way as in the simulation experiments, without the downsampling. To enhance
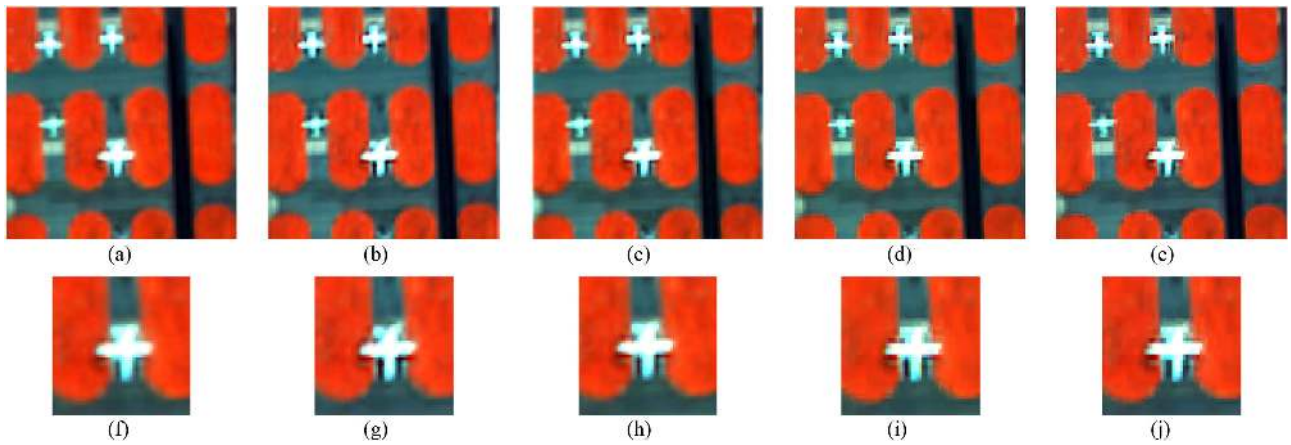
Fig. 12. Different super-resolution results obtained with Real data set 1. (a) Bilinear. (b) AWSR. (c) TLC. (d) GP. (e) Proposed UFRM method. (f)–(j) Zoomed images corresponding to (a)–(e).
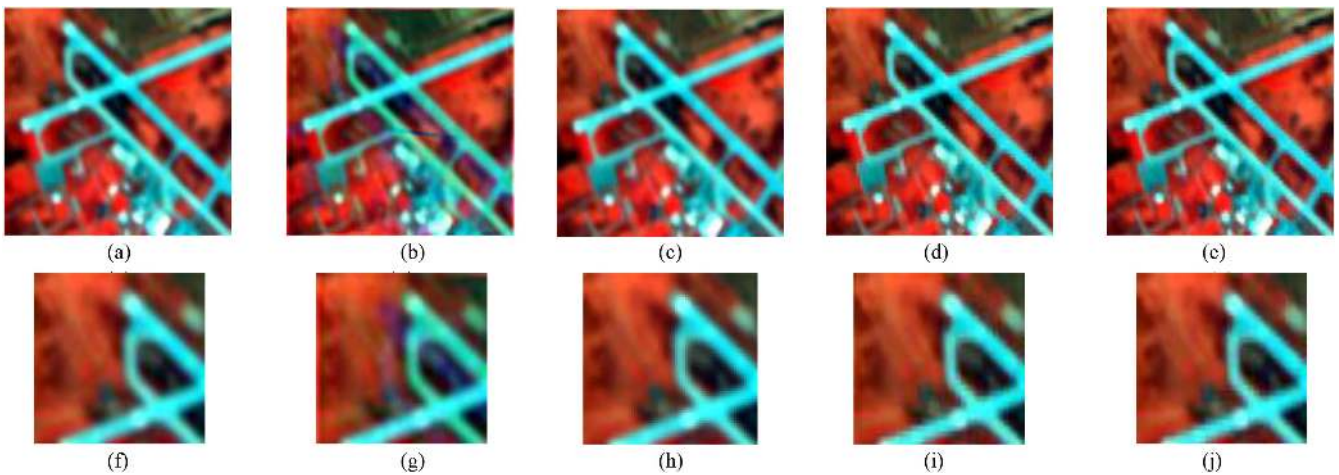


Fig. 13. Different super-resolution results obtained with Real data set 2: (a) Bilinear. (b) AWSR. (c) TLC. (d) GP. (e) proposed UFRM method. (f)–(j) zoomed images corresponding to (a)–(e).

TABLE III
CPBD EVALUATION OF THE DIFFERENT SUPER-RESOLUTION METHODS WITH THE REAL DATA

| Method | | Bilinear | AWSR | TLC | GP | Proposed UFRM method |
|---|---|---|---|---|---|---|
| Real data set 1 | CPBD | 0.1439 | 0.4264 | 0.4009 | 0.4857 | **0.5305** |
| Real data set 2 | CPBD | 0.0755 | 0.1401 | 0.1075 | 0.3260 | **0.3427** |

the difference for the visual inspection, false-color images are used to illustrate the SRR results. The reconstruction results for Real data set 1 are shown in Fig. 12. Zoomed images are shown in Fig. 12(f)–(j). From these figures, it can be seen that the resolution of the image is clearly increased after the use of the SRR technique, especially the outline of the airplane in Fig. 12(i)–(j). The reconstruction results for Real data set 2 are shown in Fig. 13. Blurring is apparent in Fig. 13(b) and Fig. 13(g), whereas the UFRM method shows a good ability to reconstruct the detailed information. The good performance of the proposed UFRM method can also be observed in the CPBD values presented in Table III. From the quantitative evaluation

provided in Table III, it can be seen that the UFRM method can obtain a stable reconstruction result, on both the multispectral images and hyperspectral images.

## IV. CONCLUSION

In this article, we have proposed a unified framework based on rank minimization (UFRM) for the joint super-resolution and registration of multiangle multi/hyperspectral remote sensing images. A multiangle multi/hyperspectral observation model is established, and each observed image is decomposed into a background image and a foreground image. A MTV regularization

term is further added to improve the image quality, considering the high correlation between the different bands of the multi/hyperspectral images. An alternating minimization strategy is utilized to resolve the joint cost function, which integrates the unknown image registration transformation parameters and the desired reconstruction image at the same time. The advantage of this algorithm is that the image registration parameters and the desired reconstruction image can be iteratively updated in a mutually beneficial manner. The main contribution of the proposed method is that it exploits the spectral information of multiangle remote sensing images for SRR, where the spectral information of the multi/hyperspectral remote sensing images is treated as an entirety, rather than band-by-band. The experimental results showed that the proposed UFRM method performs better than the traditional SRR methods, from both visual inspections and quantitative assessments. However, there is room for further improvement. For example, how to adaptively determine the regularization parameters will be investigated in our future work.

## REFERENCES

[1] M. Li, L. K. Kwoh, C. Yang, and S. C. Liew, "3D building extraction with semi-global matching from stereo pair worldview-2 satellite imageries," in *Proc. IEEE Int. Geosci. Remote Sens. Symp.*, 2015, pp. 3006–3009.

[2] M. Hashim and K. Deilami, "Very high resolution optical satellites for DEM generation: A review," *Eur. J. Sci. Res.*, vol. 49, no. 4, pp. 542—554, 2011.

[3] N. Longbotham, C. Chaapel, L. Bleiler, C. Padwick, W. J. Emery, and F. Pacifici, "Very high resolution multiangle urban classification analysis," *IEEE Trans. Geosci. Remote Sens.*, vol. 50, no. 4, pp. 1155–1170, Apr. 2012.

[4] X. Huang, H. Chen, and J. Gong, "Angular difference feature extraction for urban scene classification using ZY-3 multi-angle high-resolution satellite imagery," *ISPRS J. Photogramm. Remote Sens.*, vol. 135, pp. 127–141, 2018.

[5] T. Liu and A. Abd-Elrahman, "Deep convolutional neural network training enrichment using multi-view object-based analysis of unmanned aerial systems imagery for wetlands classification," *ISPRS J. Photogramm. Remote Sens.*, vol. 139, pp. 154–170, 2018.

[6] G. Matasci, N. Longbotham, F. Pacifici, M. Kanevski, and D. Tuia, "Understanding angular effects in VHR imagery and their significance for urban land-cover model portability: A study of two multi-angle in-track image sequences," *ISPRS J. Photogramm. Remote Sens.*, vol. 107, pp. 99–111, 2015.

[7] Z. Huang, G. Cheng, H. Wang, H. Li, L. Shi, and C. Pan, "Building extraction from multi-source remote sensing images via deep deconvolution neural networks," *Int. Geosci. Remote Sens. Symp.*, vol. 2016-Nov., pp. 1835–1838, 2016.

[8] C. Liu, X. Huang, Z. Zhu, H. Chen, X. Tang, and J. Gong, "Automatic extraction of built-up area from ZY3 multi-view satellite imagery: Analysis of 45 global cities," *Remote Sens. Environ.*, vol. 226, no. Apr., pp. 51–73, 2019.

[9] H. Chen, X. Huang, C. Liu, J. Li, and J. Gong, "A novel building detection method using ZY-3 multi-angle imagery over urban areas," *Int. Geosci. Remote Sens. Symp.*, vol. 2018, pp. 1272–1275, 2018.

[10] X. Huang, D. Wen, J. Li, and R. Qin, "Multi-level monitoring of subtle urban changes for the megacities of China using high-resolution multi-view satellite imagery," *Remote Sens. Environ.*, vol. 196, pp. 56–75, 2017.

[11] L. Yue, H. Shen, J. Li, Q. Yuan, H. Zhang, and L. Zhang, "Image super-resolution: The techniques, applications, and future," *Signal Process.*, vol. 128, pp. 389–408, 2016.

[12] T. S. Huang and R. Y. Tsai, "Multi-frame image restoration and registration," *Adv. Comput. Vis. Image Process.*, vol. 1, pp. 317–339, 1984.

[13] R. R. Schultz and R. L. Stevenson, "Extraction of high-resolution frames from video sequences," *IEEE Trans. Image Process.*, vol. 5, no. 6, pp. 996–1011, 1996.

[14] R. C. Hardie and D. R. Droege, "A MAP estimator for simultaneous superresolution and detector nonunifomity correction," *EURASIP J. Adv. Signal Process.*, vol. 2007, 2007.

[15] H. Stark and P. Oskoui, "High-resolution image recovery from image-plane arrays, using convex projections," *J. Opt. Soc. Amer. A*, vol. 6, no. 11, p. 1715, 1989.

[16] H. Ur and D. Gross, "Improved resolution from subpixel shifted pictures," *CVGIP Graph. Model. Image Process.*, vol. 54, no. 2, pp. 181–186, 1992.

[17] B. C. Tom and A. K. Katsaggelos, "Reconstruction of a high-resolution image by simultaneous registration, restoration, and interpolation of low-resolution images," *IEEE Int. Conf. Image Process.*, vol. 2, no. 6, pp. 539–542, 1996.

[18] M. Irani and S. Peleg, "Improving resolution by image registration," *CVGIP: Graphical Models Image Process.*, vol. 53, no. 3, pp. 231–239, 1991.

[19] M. Elad and A. Feuer, "Restoration of a single superresolution image from several blurred, noisy, and undersampled measured images," *IEEE Trans. Image Process.*, vol. 6, no. 12, pp. 1646–1658, Dec. 1997.

[20] C. Latry and B. Rougé, "Super resolution: Quincunx sampling and fusion processing," *Int. Geosci. Remote Sens. Symp.*, vol. 1, no. C, pp. 315–317, 2003.

[21] H. Zhang, Z. Yang, L. Zhang, and H. Shen, "Super-resolution reconstruction for multi-angle remote sensing images considering resolution differences," *Remote Sens.*, vol. 6, no. 1, pp. 637–657, 2013.

[22] H. Shen, M. K. Ng, P. Li, and L. Zhang, "Super-resolution reconstruction algorithm to MODIS remote sensing images," *Comput. J.*, vol. 52, no. 1, pp. 90–100, 2009.

[23] F. Li, X. Jia, D. Fraser, and A. Lambert, "Super resolution for remote sensing images based on a universal hidden Markov tree model," *IEEE Trans. Geosci. Remote Sens.*, vol. 48, no. 3, pp. 1270–1278, Mar. 2010.

[24] H. Chen, H. Zhang, and L. Zhang, "Robust superresolution of multiangle-multispectral remote sensing images based on rank minimization," in *Proc. Int. Geosci. Remote Sens. Symp.*, 2016, vol. 2016-Nov., pp. 7264–7267.

[25] S. Leprince, S. Barbot, F. Ayoub, and J. P. Avouac, "Automatic and precise orthorectification, coregistration, and subpixel correlation of satellite images, application to ground deformation measurements," *IEEE Trans. Geosci. Remote Sens.*, vol. 45, no. 6, pp. 1529–1558, Jun. 2007.

[26] J. Ma, J. C. W. Chan, and F. Canters, "Fully automatic subpixel image registration of multiangle CHRIS/Proba data," *IEEE Trans. Geosci. Remote Sens.*, vol. 48, no. 7, pp. 2829–2839, Jul. 2010.

[27] T. Hu, H. Zhang, H. Shen, and L. Zhang, "Robust registration by rank minimization for multiangle hyper/multispectral remotely sensed imagery," *IEEE J. Sel. Topics Appl. Earth Observ. Remote Sens.*, vol. 7, no. 6, pp. 2443–2457, Jun. 2014.

[28] H. Shen, L. Zhang, B. Huang, and P. Li, "A MAP approach for joint motion estimation, segmentation, and super resolution," *IEEE Trans. Image Process.*, vol. 16, no. 2, pp. 479–490, Feb. 2007.

[29] M. Amintoosi, M. Fathy, and N. Mozayani, "Precise image registration with structural similarity error measurement applied to superresolution," *EURASIP J. Adv. Signal Process.*, vol. 2009, 2009, Art. no. 305479.

[30] X. Wang, Y. Li, H. Wei, and F. Liu, "An ASIFT-based local registration method for satellite imagery," *Remote Sens.*, vol. 7, no. 6, pp. 7044–7061, 2015.

[31] A. Laghrib, A. Hadri, A. Hakim, and S. Raghay, "A new multiframe super-resolution based on nonlinear registration and a spatially weighted regularization," *Inf. Sci. (Ny).*, vol. 493, pp. 34–56, 2019.

[32] J. C. W. Chan, J. Ma, P. Kempeneers, and F. Canters, "Superresolution enhancement of hyperspectral CHRIS/Proba images with a thin-plate spline nonrigid transform model," *IEEE Trans. Geosci. Remote Sens.*, vol. 48, no. 6, pp. 2569–2579, Jun. 2010.

[33] L. Li, W. Wang, H. Luo, and S. Ying, "Super-resolution reconstruction of high-resolution satellite ZY-3 TLC images," *Sensors*, vol. 17, no. 5, 2017.

[34] J. Ma, J. Cheung-Wai Chan, and F. Canters, "An operational superresolution approach for multi-temporal and multi-angle remotely sensed imagery," *IEEE J. Sel. Topics Appl. Earth Observ. Remote Sens.*, vol. 5, no. 1, pp. 110–124, Feb. 2012.

[35] J. Ma, J. C. W. Chan, and F. Canters, "Robust locally weighted regression for superresolution enhancement of multi-angle remote sensing imagery," *IEEE J. Sel. Topics Appl. Earth Observ. Remote Sens.*, vol. 7, no. 4, pp. 1357–1371, Apr. 2014.

[36] A. E. Galbraith, J. Theiler, K. J. Thome, and R. W. Ziolkowski, "Resolution enhancement of multilook imagery for the multispectral thermal imager," *IEEE Trans. Geosci. Remote Sens.*, vol. 43, no. 9, pp. 1964–1976, Sep. 2005.

[37] H. Zhang, L. Zhang, and H. Shen, "A blind super-resolution reconstruction method considering image registration errors," *Int. J. Fuzzy Syst.*, vol. 17, no. 2, pp. 353–364, 2015.

[38] G. Puy and P. Vandergheynst, "Robust image reconstruction from multi-view measurements," *SIAM J. Imag. Sci.*, vol. 7, pp. 128–156, 2014.

[39] Q. Cheng, H. Shen, L. Zhang, and P. Li, "Inpainting for remotely sensed images with a multichannel nonlocal total variation model," *IEEE Trans. Geosci. Remote Sens.*, vol. 52, no. 1, pp. 175–187, Jan. 2014.

[40] Q. Yuan, L. Zhang, H. Shen, and P. Li, "Adaptive multiple-frame image super-resolution based on U-curve," *IEEE Trans. Image Process.*, vol. 19, no. 12, pp. 3157–3170, Dec. 2010.

[41] P. Blomgren and T. F. Chan, "Color TV: Total variation methods for restoration of vector-valued images," *IEEE Trans. Image Process.*, vol. 7, no. 3, pp. 304–309, Mar. 1998.

[42] Q. Yuan, L. Zhang, and H. Shen, "Hyperspectral image denoising employing a spectral–spatial adaptive total variation model," *IEEE Trans. Geosci. Remote Sens.*, vol. 50, no. 10, pp. 3660–3677, Oct. 2012.

[43] H. Attouch, J. Bolte, P. Redont, and A. Soubeyran, "Proximal alternating minimization and projection methods for nonconvex problems: An approach based on the Kurdyka-Lojasiewicz inequality," *Math. Oper. Res.*, vol. 35, no. 2, pp. 438–457, 2010.

[44] S. Sra, S. Nowozin, and S. Wright, Optimization for machine learning, vol. 53, no. 9. 2012.

[45] F. Pacifici and Q. Du, "Foreword to the special issue on optical multiangular data exploitation and outcome of the 2011 GRSS data fusion contest," *IEEE J. Sel. Topics Appl. Earth Observ. Remote Sens.*, vol. 5, no. 1, pp. 3–7, Feb. 2012.

[46] L. Alonso and J. Moreno, "Advances and limitations in a parametric geometric correction of CHRIS/Proba data," *Eur. Sp. Agency, (Special Publ. ESA SP)*, vol. 593, pp. 7–13, 2005.

[47] Z. Wang, A. C. Bovik, H. R. Sheikh, and E. P. Simmoncelli, "Image quality assessment: Form error visibility to structural similarity," *IEEE Trans. Image Process.*, vol. 13, no. 4, pp. 600–612, Apr. 2004.

[48] L. Alparone, L. Wald, J. Chanussot, C. Thomas, P. Gamba, and L. M. Bruce, "Comparison of pansharpening algorithms: Outcome of the 2006 GRS-S data-fusion contest," *IEEE Trans. Geosci. Remote Sens.*, vol. 45, no. 10, pp. 3012–3021, Oct. 2007.

[49] N. D. Narvekar and L. J. Karam, "A no-reference perceptual image sharpness metric based on a cumulative probability of blur detection," in *Proc. Int. Work. Qual. Multimed. Exp.*, 2009, vol. 20, no. 9, pp. 87–91.

**Hongyan Zhang** (Senior Member, IEEE) received the B.S. degree in geographic information systems and the Ph.D. degree in photogrammetry and remote sensing from Wuhan University, China, in 2005 and 2010, respectively.

Since 2016, he has been a Full Professor with the State Key Laboratory of Information Engineering in Surveying, Mapping, and Remote Sensing, Wuhan University. His research interests include image reconstruction for quality improvement, hyperspectral information processing, and agricultural remote sensing. He is a Young Chang-Jiang Scholar appointed by the Ministry of Education of China. He was the recipient of the 1st place in the Pairwise Semantic Stereo Challenge of the 2019 Data Fusion Contest organized by the IEEE Image Analysis and Data Fusion Technical Committee. He has authored/co-authored more than 90 research papers.

Dr. Zhang is an Associate Editor with *Photogrammetric Engineering & Remote Sensing and Computers Geosciences*, and was the Session Chair of the 2016 IEEE IGARSS conference, and the 2015 IEEE WHISPERS conference. He is a reviewer for more than 30 international academic journals, including IEEE TRANSACTIONS ON GEOSCIENCE AND REMOTE SENSING, IEEE TRANSACTIONS ON IMAGE PROCESSING, IEEE JOURNAL OF SELECTED TOPICS IN APPLIED EARTH OBSERVATIONS AND REMOTE SENSING, and IEEE GEOSCIENCE AND REMOTE SENSING LETTERS.

**Juan Du** received the Ph.D. degree in photogrammetry and remote sensing from Wuhan University, China, in 2008, where she is currently a Lecturer with the School of Remote Sensing and Information Engineering. Her research interests focus on remote sensing applications and remote sensing image processing.

**Hang Chen** received the B.S. degree from Wuhan University, Wuhan, China, in 2013, where he is currently working toward to the Ph.D. degree with The State Key Laboratory of Information Engineering in Surveying, Mapping and Remote Sensing.

He is currently part of the High-resolution intelligent information Processing and Application Group (HiPAG). His research interests include remote sensing image processing, machine learning, and applications of multiview remote sensing images.

**Bin Luo** received the M.Sc. degree from ENS Cachan, France, in 2003 and the Ph.D. degree from ENST Paris, France, in 2007. From 2008 to 2010, he was a Post-Doctoral Researcher with GIPSA-Lab, France. He is currently a Professor with the State Key Laboratory of Information Engineering in Surveying, Mapping and Remote Sensing (LIESMARS), Wuhan University, China. His research interests include hyperspectral data analysis and high-resolution remote sensing image processing.